

Spark-Plasma Sintering of W-5.6Ni-1.4Fe Heavy Alloys: Densification and Grain Growth

KE HU, XIAOQIANG LI, SHENGGUAN QU, and YUANYUAN LI

W-5.6Ni-1.4Fe heavy alloys were prepared by the method of spark-plasma sintering, and the densification and grain growth kinetics were analyzed as a function of various parameters such as sintering temperature and dwell duration. It is found that the local temperature gradient at the vicinity of the pores can cause the matrix phase melting or softening, resulting in a viscous layer coating the W particles and an improved solubility of W into the matrix phase. In the initial stage, particle rearrangement and neck formation and growth take place, and γ -(Ni, Fe) matrix phase has formed. Dissolution-precipitation and Ni-enhanced W grain boundary diffusion together with viscous process contribute to the simultaneous densification and grain growth in the intermediate stage. During the final stage, fast grain growth, controlled by both gas-phase diffusion and dissolution-precipitation mechanisms, dominates over the densification.

DOI: 10.1007/s11661-012-1454-4

© The Minerals, Metals & Materials Society and ASM International 2012

I. INTRODUCTION

W-Ni-Fe heavy alloys are typical two-phase composites used in the applications requiring high density, such as kinetic energy penetrators, counter weights, and radiation shields.^[1-3] Generally, the alloys are liquid sintered from blended elemental powders of tungsten, nickel, and iron at a temperature above 1733 K (1460 °C).^[4] After sintering, the microstructure consists of coarsened spherical body-centered cubic tungsten grains dispersed in a face-centered cubic (fcc) Ni-Fe-W solid-solution matrix.^[5]

In the past decades, many investigators have presented that the fine-grain microstructure can improve the mechanical properties of tungsten heavy alloys.^[6-10] In order to refine microstructure, lots of research papers focused on adding inhibitors to prevent the grain growth. Recent literature has reported that adding a trace amount of rare earth elements or their oxides can refine the grain size and enhance the penetration performance of tungsten heavy alloys.^[11-14] Some researchers adopted high-energy ball milling (HEBM) combining with novel sintering technologies, such as two-stage sintering, microwave sintering, and electric current activated sintering, to prepare ultrafine grained heavy alloys or tungsten.^[2,15-18] Spark-plasma sintering (SPS), often referred to as field-assisted sintering technique (FAST) or pulsed electric current sintering (PECS), is a newly arisen sintering technique that employs a pulsed direct current (DC) to powders subject to a modest applied pressure (<100 MPa). High electrical current application enables a fast heating rate (up to 1000 K min⁻¹ [1000 °C min⁻¹]),

resulting in a very short sintering cycle, typically a few minutes for full densification of both conductive and nonconductive powders.^[19,20] Thereby, a high densification rate is favored while grain coarsening induced by surface diffusion is minimized, and then grain growth can be suppressed.

In a previous paper,^[21] we reported investigation on the effect of heating rate on the densification behavior and the microstructure evolution of W-Ni-Fe heavy alloys. The aims of this study are, first, to use the SPS method to prepare bulk W-Ni-Fe heavy alloys from blended elemental powders and study the influence of various SPS parameters (sintering temperature and dwell duration) on the densification and grain growth of the powders, and second, to perform a formal sintering analysis in order to help formulate a hypothesis concerning the mechanism(s) that controls densification and grain growth.

II. EXPERIMENTAL PROCEDURE

Commercial tungsten, nickel, and iron elemental powders were selected for this study. The characteristics of the raw powders are shown in Table I. W, Ni, and Fe powders were weighed accurately to make up a desired stoichiometric composition of 93.00 pct W-5.60 pct Ni-1.40 pct Fe (wt pct). The weighed powders were subsequently blended for 10 hours. Figure 1 shows the scanning electron micrograph (SEM) of the homogeneously blended powders.

The blended powders were sintered by SPS (Dr. Sinter825, Sumitomo Coal Mining Co. Ltd., Tokyo, Japan) in a 20.4-mm inner diameter graphite die. Graphite foils of 0.2 mm thickness were placed between the punches and the powders, and between the die and the powders for easy removal and significant reduction of temperature inhomogeneities. In addition, the exterior of the die was covered by graphite felt with a thickness of ~10 mm, which was used as a thermal insulation to reduce the

KE HU, Ph.D. Candidate, and XIAOQIANG LI, SHENGGUAN QU, and YUANYUAN LI, Professors, are with the National Engineering Research Center of Near-Net-Shape Forming for Metallic Materials, South China University of Technology, Guangzhou 510640, P.R. China. Contact e-mail: Lixq@scut.edu.cn.

Manuscript submitted February 29, 2012.

Article published online October 11, 2012

Table I. Characteristics of the Raw Powders

Elemental Powder	Purity (Pct)	Average Particle Size (μm)	Main Impurity (Wt pct)			
			C	O	P	N
W	99.92	2.44	0.002	0.07	0.0008	—
Ni	99.5	2.64	≤ 0.25	≤ 0.11	0.0003	—
Fe	99.5	6.05	≤ 0.1	≤ 0.3	—	≤ 0.1

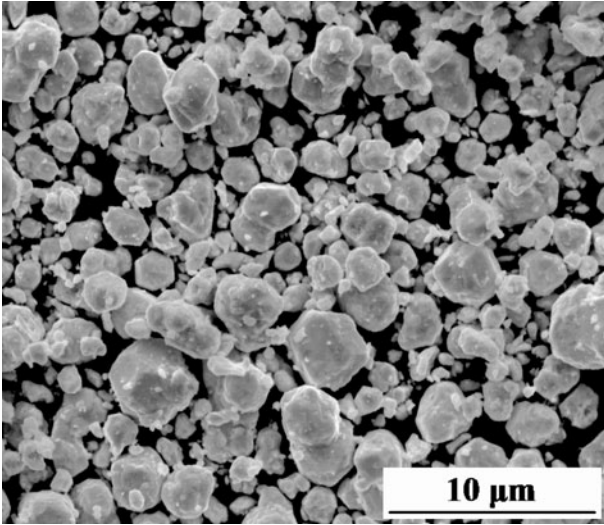


Fig. 1—SEM micrograph of the blended powders.

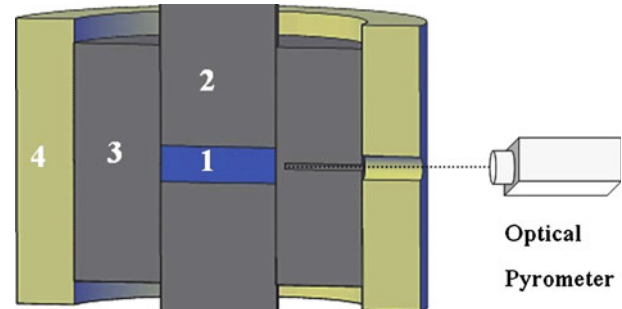


Fig. 2—Schematic of the graphite die-punches assembly: 1—specimen, 2—graphite punch, 3—graphite female die, and 4—graphite felt.

radiation losses and possible temperature gradients.^[22,23] Sintering was performed in vacuum (residual cell pressure < 8 Pa), and a constant pressure of 30 MPa was applied from the beginning of the heating step to the end of the dwell. The pulses pattern was constant and it consisted of 12 pulses (with a pulse duration of 3.3 ms) followed by two periods of zero current, which was termed as 12:2 for the pulse sequence. An optical pyrometer, focused on the bottom of a small blind hole (with a diameter of 2 mm and a distance of 1.5 mm away from the inner wall of the female die), which was drilled in the external die wall at the same height as the center of the powder compact, was used to measure and adjust the temperature. The schematic of the graphite die-punches assembly was shown in Figure 2. For all sintering, the heating from room temperature to 873 K (600 °C) was controlled by a preset heating program and completed within 4 minutes. From 873 K (600 °C) to the desired temperature, a heating rate of 90 K min⁻¹ (90 °C min⁻¹) was used. When the required temperature was reached, the sample was then soaked for 0 to 45 minutes. The chosen dwell temperature range was between 1233 K and 1593 K (960 °C and 1320 °C).

All of the sintered specimens were ground and polished to remove any surface graphite contamination. Then, the sintered density was determined by the Archimedes' method. The final relative density was obtained using the apparent volume mass divided by the theoretical value of 17.71 g cm⁻³. The microstructure of specimens taken from polished plane or fracture surfaces was examined by SEM (Quanta 200, FEI Corporation, Hillsboro, OR),

equipped with an energy-dispersive spectrometer (EDS) analysis system (INCA PentaFET-x3, Oxford Instruments, Oxfordshire, U.K.). The polished specimens were chemically etched with a solution of 6 g of potassium ferricyanate and 0.5 g of potassium hydroxide in 50 mL distilled water^[24] to observe the microstructure and quantify the grain size. At the same time, the average grain size was measured from SEM graphs taken from a polished plane using a line-intercept method and taking into account of at least 400 grains (with a three-dimensional correction factor determined to be 1.571^[25]). Phase identification was conducted by an X-ray diffractometer (XRD; D8 Advance; Bruker AXS Co., Karlsruhe, Germany) using Cu K α radiation. The contents of W, Ni, and Fe in the matrix phase were detected by EDS. The final measurement results were the average of eight tested values taken from different areas.

III. RESULTS

A. Densification Behavior and Microstructural Features

Figure 3 shows the densification curves obtained for the different dwell temperatures selected. It appears clearly that at the low SPS temperature ranging from 1233 K to 1413 K (960 °C to 1140 °C), the longer the dwell time, the higher the relative density of the sintered specimen. As the temperature increases to 1503 K (1230 °C), the relative density increases sharply from 0.83 to 0.96 after 5 minutes duration, followed by a slight decrease with the dwell time further increasing. When sintering is done at a higher temperature [1593 K (1320 °C)], the relative density reaches 0.96 without duration and also decreases slightly with the increase of dwell time.

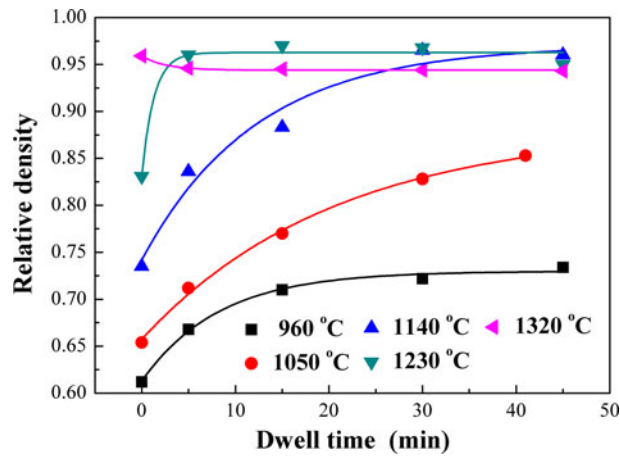


Fig. 3—Densification curves obtained for different SPS temperatures as a function of the dwell time. The heating rate was fixed at 90 K min^{-1} ($90 \text{ }^\circ\text{C min}^{-1}$) and the applied macroscopic compaction pressure was a constant of 30 MPa.

During SPS process, the shrinkage of the powder beds was determined from the punch displacement. Considering the thermal expansion of sample, graphite die and graphite spacers, baselines were done experimentally to correct the original punch displacement. For this correction, which was explained in Reference 26, the baseline was recorded by heating a full dense specimen with heating rate of 90 K min^{-1} ($90 \text{ }^\circ\text{C min}^{-1}$) and pressure of 30 MPa. Figure 4 shows the experimental and corrected shrinkage displacement and the corresponding baseline, as well as the corrected shrinkage rate during sintering W-Ni-Fe powders to 1593 K (1320 °C).

According to the corrected shrinkage curve and the corresponding shrinkage rate coupled with the microstructure evolution as shown in Figure 5, the whole densification process can be divided into four parts, which are denoted with Roman numbers (in Figure 4). It should be stated that the way of dividing is rather arbitrary and the boundaries between each part are actually not clear and difficult to define. However, such a treatment helps to produce a profound analysis and it may yield an instructive insight into the SPS mechanism. During the early stage of the SPS process (part I in Figure 4), being below 1143 K (870 °C), the specimen experiences a small amount of densification probably due to particle rearrangement resulting from the effect of the pressure. Compared with the blended powders, there is no distinct change in the microstructure of W-Ni-Fe powders heated to 1143 K (870 °C) as shown in Figure 5(a), but the relative density slightly increases from 0.53 ± 0.01 to 0.56 ± 0.01 . Part II is characterized by the sintering neck formation and growth, in which the temperature ranges from 1143 K to 1323 K (870 °C to 1050 °C). Recently, Aman *et al.*^[27] and Cordier *et al.*^[28] have presented some evidence of mass transport in the neck formation by an ejection mechanism or protrusion formation during the SPS of spherical Cu powders and yttrium-doped zirconia granules, respectively. However, in our study, no similar phenomenon was detected. In this part, necks develop between W particles (as shown in

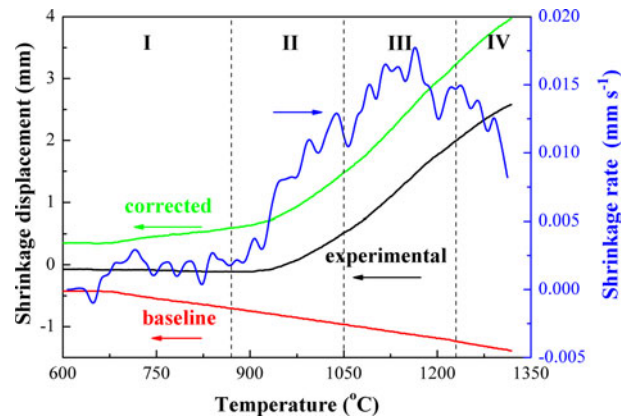


Fig. 4—Experimental and corrected shrinkage displacement and the corresponding baseline, as well as the corrected shrinkage rate during sintering of W-Ni-Fe powders as a function of the SPS temperature (under a pressure of 30 MPa).

Figures 5(b) and (c)), making possible the contribution of W grain boundary diffusion to the densification of the material. The contribution of a pressure-applied mechanism (*i.e.*, power-law creep) to the grain-boundary diffusion can also lead to an enhanced mass transport during neck growth.^[29] In addition, the mechanisms of electromigration^[30] and/or reduction of oxide surface from evaporation^[31] lead to an enhanced neck growth due to the effect of the pulsed current and have been observed during the SPS of Cu and W, respectively. On the other hand, from the XRD patterns shown in Figure 6, we can see that the γ -(Ni, Fe) matrix phase has formed at 1233 K (960 °C). According to the literature,^[32] Ni and Fe are ensured to have low activation energies for grain boundary diffusion and lattice diffusion, and consequently a fcc solid solution or γ -(Ni, Fe) matrix phase is formed at low temperature by these mechanisms and their interdiffusion. Therefore, an increase in density to ~ 0.65 of the theoretical takes place. For the temperature in the range of 1323 K to 1503 K (1050 °C to 1230 °C), Part III covers the major part of the densification process. In this part, the shrinkage rate rapidly increases with the increase of temperature and reaches a maximum at $\sim 1423 \text{ K}$ (1150 °C). The corresponding microstructure evolution is shown in Figure 5(d) and (e). Densification is evident in the micrographs with the increase of the temperature. Table II shows the EDS results of the contents of W, Ni, and Fe in the matrix phase. It is noteworthy that when the temperature increases, the ratio of Ni to Fe tends to be stable, approaching to 4. From the micrograph presented on the top right of Figure 5(d), the matrix phase spreads on the surface of W particles by diffusion or possible viscous flow. As a result, the matrix phase fills the pores between W particles improving specimens' density. Furthermore, it is interesting that the solubility of W in the matrix phase almost remains a constant (about 32 wt pct) regardless of the sintering temperature. Our results are evidently different from that of Chausse, in which it is found that the solubility of W in the matrix phase is very small when the temperature is lower than 1473 K (1200 °C), and then it increases with the temperature and becomes stable (about 30 wt pct)

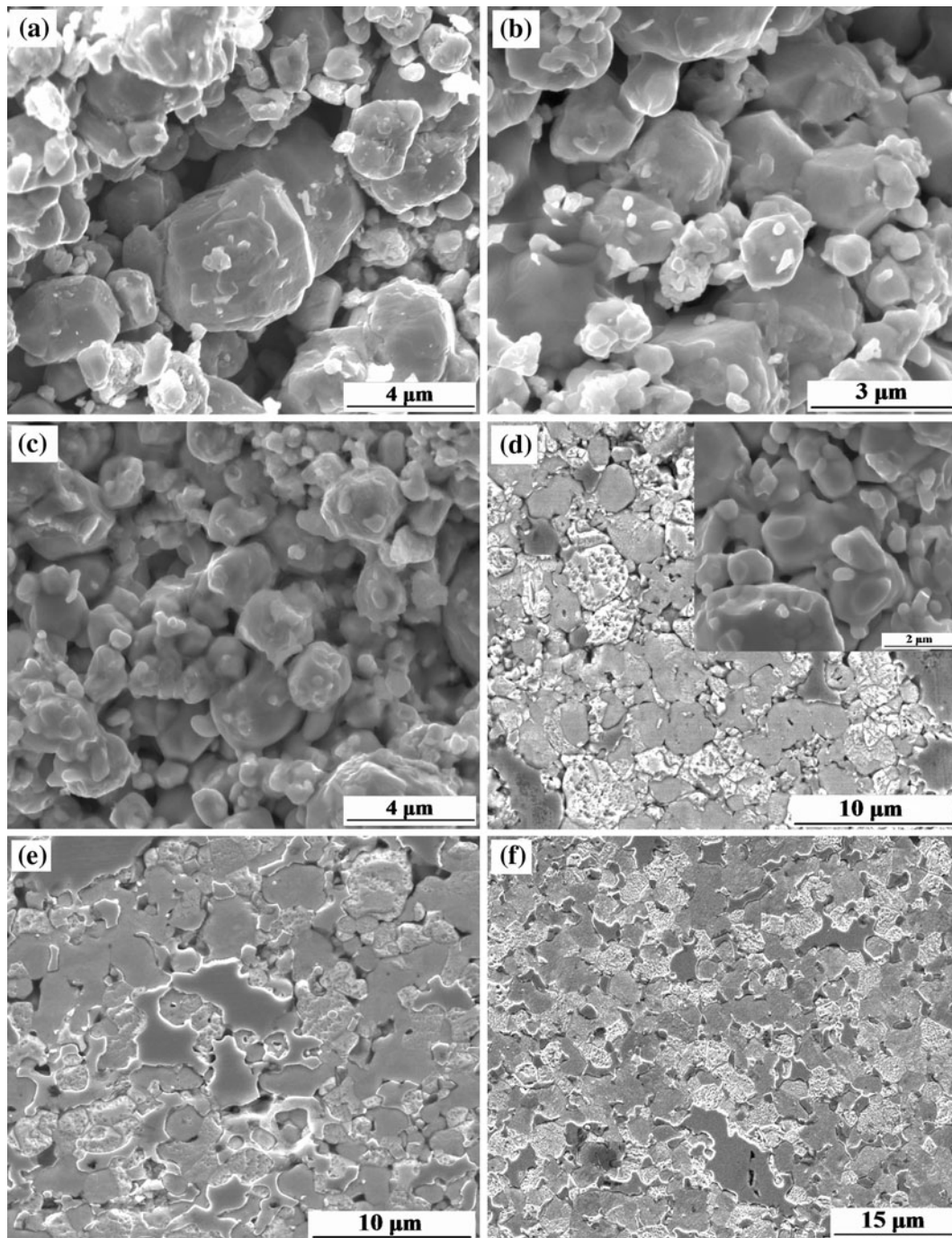


Fig. 5—SEM graphs of the microstructure of W-Ni-Fe SPS at different temperatures without duration and with a heating rate fixed at 90 K min^{-1} ($90 \text{ }^\circ\text{C min}^{-1}$) and a constant pressure of 30 MPa: (a) 1143 K ($870 \text{ }^\circ\text{C}$), (b) 1233 K ($960 \text{ }^\circ\text{C}$), (c) 1323 K ($1050 \text{ }^\circ\text{C}$), (d) 1413 K ($1140 \text{ }^\circ\text{C}$), (e) 1503 K ($1230 \text{ }^\circ\text{C}$), and (f) 1593 K ($1320 \text{ }^\circ\text{C}$).

above 1673 K ($1400 \text{ }^\circ\text{C}$).^[33] Otherwise, the graphs show that W grains are rounded with grain growth at higher temperatures. Therefore, densification is promoted by a dissolution–precipitation mechanism. In part IV, the densification rate decreases gradually, but the density continues to increase. For 1593 K ($1320 \text{ }^\circ\text{C}$), the relative density is 0.96 without duration (the corresponding microstructure as shown in Figure 5(f)). Further increasing the temperature (not shown here) or the dwell time at 1593 K ($1320 \text{ }^\circ\text{C}$), the relative density does not increase

continuously (Figure 3); however, W grains coarsen rapidly (see the next section).

B. Grain Growth and Sintering Trajectory

Figure 7 shows the variation of W grain size as a function of dwell time for the different dwell temperatures. At a low sintering temperature [1233 K ($960 \text{ }^\circ\text{C}$)], negligible grain growth is observed. As increasing temperatures from 1323 K to 1593 K ($1050 \text{ }^\circ\text{C}$ to

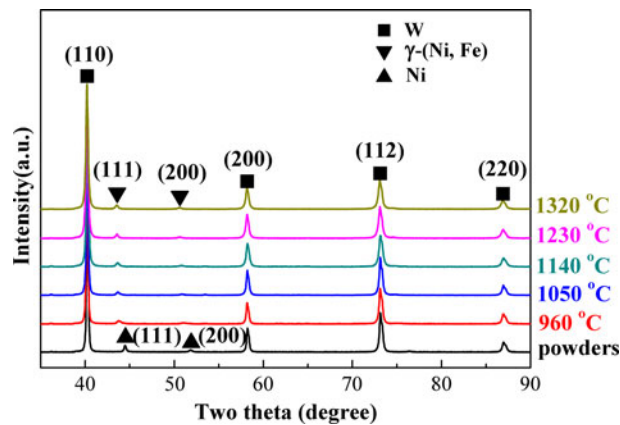


Fig. 6—XRD patterns of blended powders and specimens sintered at various temperatures.

Table II. Contents of W, Ni, and Fe in the γ Matrix Phase at Different Sintering Temperature with 5-Min Duration

Temperature [K (°C)]	Contents of W, Ni, and Fe in the γ Matrix Phase (Wt pct)		
	W	Ni	Fe
1323 (1050)	32.60	57.54	9.86
1413 (1140)	32.08	56.75	11.17
1503 (1230)	32.87	54.63	12.50
1593 (1320)	32.79	53.07	14.14

1320 °C), grain growth occurs with the increase of dwell duration. Furthermore, the grain size increases moderately at the lower temperature [*i.e.*, 1323 K (1050 °C)] compared to the higher temperature range [*i.e.*, 1503 K to 1593 K (1230 °C to 1320 °C)]. The different grain growth behavior at the two temperature ranges reveals the corresponding different densification and grain growth mechanisms. Figure 8 shows the sintering trajectory of SPS W-Ni-Fe heavy alloys, with average W grain size plotted as a function of relative density. Apparently, the whole densification process covers three sequential stages referred to as (1) the initial stage, (2) the intermediate stage, and (3) the final stage. In the initial stage, specimens' relative density increases from initial 0.53 to approximately 0.60 to 0.65 without grain growth. It is interesting that during the intermediate stage, the average grain size increases slowly and roughly linearly with the relative density up to ~0.95, but then it increases much more rapidly above this relative density value in the final stage. In the next section, the nature of sintering mechanisms and kinetics during these three stages will be analyzed and discussed by using classic kinetics laws.

IV. DISCUSSION

SPS densification mechanisms have been classically analyzed by considering the major driving sources of densification-contributing mass transfer such as: (1)

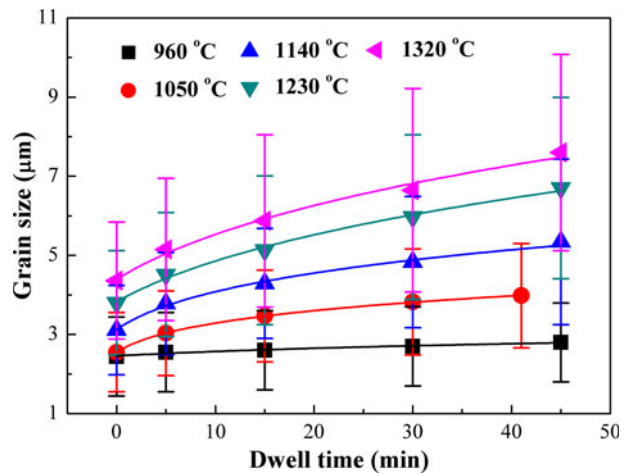


Fig. 7—Grain growth curves obtained for different SPS temperatures as a function of the dwell time. The heating rate was fixed at 90 K min⁻¹ (90 °C min⁻¹) and the applied macroscopic compaction pressure was a constant of 30 MPa.

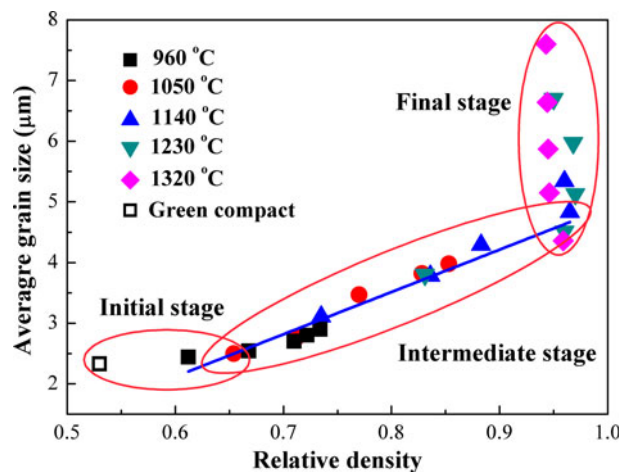


Fig. 8—The average grain size vs relative density trajectory of SPS W-Ni-Fe heavy alloy. The heating rate was fixed at 90 K min⁻¹ (90 °C min⁻¹) and a constant pressure of 30 MPa was applied.

externally applied load, (2) sintering stress (*i.e.*, surface tension), (3) steady-state electromigration (*i.e.*, electric field contribution to diffusion), and (4) presence of momentarily generated spark plasma between particles.^[34]

In several research reports, as we know, the notion of the existence of plasma in SPS is only repeated routinely. There is not yet sufficient evidence to illustrate the plasma generation in the current study. Let us assume that the application of the high-pulsed DC current induces extraordinarily high local temperature at particle surfaces, resulting in softening or melting of nickel and iron. Seeing the fracture surface as shown in Figure 5, the W particle surfaces contain a viscous layer. It is documented that the diffusivity of tungsten in the matrix goes up several orders of magnitude after melting.^[32] Thus, we have confidence to believe that the diffusion rate accelerates in the viscous layer and the densification is promoted. In the current investigation, for the sake of simplification,

we assume that the electric field contribution (electromigration) is to improve the dissolution rate of the W grains into the γ -(Ni, Fe) matrix. Otherwise, the sintering stress, which depends on the level of grain-pore and grain-grain interface areas in the considered material, becomes an insignificant term when the applied load is large enough. Therefore, the densification during SPS of the W-Ni-Fe heavy alloys is similar to that of the hot pressing (HP), in which the mass transport by diffusion is usually the dominant mechanism.

Recently, in the comparative studies between SPS and HP of electrical insulating (α -Al₂O₃),^[35] ionic conductive (yttria-stabilized zirconia),^[36] and semiconductive materials (ZnO),^[37] Langer *et al.* concluded that densification proceeds similarly in both cases by the same diffusion mechanism. Thus, the existing analytical model of HP can be adopted to investigate the SPS densification kinetic. According to the sintering trajectory as shown in Figure 8, three stages are clearly visible, even though the boundaries between the adjacent stages are indistinct or even overlapping. In what follows, the densification and grain growth mechanisms in each stage are analyzed and discussed.

A. Initial Stage

According to the above-mentioned results, particle rearrangement and neck formation and growth are dominating in this stage. Due to the inaccuracy of temperature control with the optical pyrometer below 873 K (600 °C), the particle rearrangement under the uniaxial compaction stress during this stage is difficult to analyze. So this contribution is not estimated in the current investigation. As for the interparticle neck formation and growth, a classic two-sphere model consisting of mass transport by diffusion, vapor transport, plastic flow, or viscous flow has been developed for conventional free sintering.^[38] When the sintering powders are subjected to a moderate pressure (like HP), the applied pressure enhances the mass transport by lattice or boundary diffusion and plastic flow; an enhanced driving force (including both the applied pressure and surface energy) for neck growth has been deduced by Coble.^[39] For the case of SPS, similarly to HP, neck growth is enhanced by pressure application as recently shown by Demirskyi *et al.*^[29] Langer *et al.*^[35] have argued that the temperature overshoot induces a higher number of necks during the initial stage of SPS in contrast to HP. Wang *et al.*^[40] have also shown that SPS enhances neck growth and accelerates the atom diffusion compared with HP. Furthermore, the unique “SPS effect” (such as favorable local conditions at the particle contacting zones consisting of local melting,^[41] local thermal breakdown^[27,42] and activation of particle surface^[31,43,44]) and electromigration^[30,45] can offer an additional contribution for neck formation and growth. However, all these results make us realize that the initial stage during SPS is very complicated. On the other hand, the γ -(Ni, Fe) matrix phase segregating to the W particle boundaries can also lead to an increase in atom mobility. As a result, the neck growth is enhanced. With the temperature increasing, the necks grow extensively, and then the densification process begins to enter the next stage.

B. Intermediate Stage

In this stage, densification and grain growth occur simultaneously (Figure 8). To understand the sintering process, we treat the process of densification and grain growth separately.

When moderate loads are applied and mass transport is controlled by diffusion, the densification strain rate can be described by the following general equation^[46]:

$$\frac{1}{\rho} \frac{d\rho}{dt} = \frac{HD(\phi p_a)^n}{G^m k T} \quad [1]$$

where H is a numerical constant, $D = D_0 \exp(-Q/RT)$ is the diffusion coefficient of the rate-controlling species (here, D_0 is a preexponential factor, Q is the activation energy for the diffusion process, and R is the universal gas constant), G is the grain size, k is the Boltzmann constant, T is the absolute temperature, ϕ is the stress intensification factor, p_a is the externally applied uniaxial stress, and the exponents m and n depend on the mechanism of densification. For a low-density body, the contact area between particles where stress is transmitted is small, and therefore the local stress is much higher than the macroscopic applied stress. Assuming that the heated compact is an ideal powder composed of monosize spherical particles in which neck growth occurs when the relative density $\rho < 0.90$, the stress intensification factor can be expressed as^[46]

$$\phi = \frac{(1 - \rho_0)^2}{\rho(\rho - \rho_0)^2} \quad [2]$$

where ρ is the density and ρ_0 is the initial green density (is about 0.53 ± 0.01). If negligible grain growth is assumed and temperature is kept constant, then the stress exponent n can be calculated using

$$\ln\left(\frac{1}{\rho} \frac{d\rho}{dt}\right) \propto \ln(\phi P_a) \quad [3]$$

For the specimens sintered at lower temperatures [1233 K (960 °C)], ρ is ranged between 0.60 and 0.75, while grain growth is negligible (Figure 7). A linear relationship is found in Figure 9, with a slope $n = 1.25$ (≈ 1), suggesting that the SPS densification mechanisms may be governed by diffusional processes. According to Park *et al.*,^[32] densification occurs through a combination of both the lattice diffusion of W in the matrix phase and the W grain boundary diffusion during solid-state sintering; while after melting of the matrix phase, the dissolution-precipitation of the W particles through the liquid phase is the dominant densification mechanism. In our current work, as outlined in the above-mentioned discussion, a combination of the solid-state and liquid-phase mechanisms may be active when a viscous phase spreads on the W particles.

On the other hand, Stanciu *et al.*^[47] have pointed out a charge gradient developed in the vicinity of pores. The electrical current density is higher next to large pores than next to small ones. Then, a local temperature gradient is created. The temperature gradient ∇T , which

develops in the vicinity of these pores under pulsed-field application by assuming no heat loss, can be calculated as follows:

$$\nabla T \approx \frac{1}{r_p} \sqrt{\frac{\lambda_e E^2 T_0}{2C}} \frac{T_0}{n} \Delta t \quad [4]$$

where r_p is the pore radius; λ_e ($\Omega^{-1} \text{ m}^{-1}$) is the electrical conductivity and C ($\text{J m}^{-3} \text{ K}^{-1}$) is the heat capacity, which both depend on porosity; E (V m^{-1}) is the intensity of electric field; T_0 (K) is the initial temperature; and n is the number of electrical impulses for achieving the desired sintering temperature from T_0 and Δt (s) the pulse sequence duration (ON-OFF).

The heat capacity dependent on porosity for powder materials can be approximated by (C_{fd} is the heat capacity of the fully dense materials and θ is the porosity)^[48]:

$$C(\theta, T) = (1 - \theta)C_{fd}(T) \quad [5]$$

The electrical conductivity dependent on porosity for powder materials is expressed as (λ_{efd} is the electric conductivity of the fully dense material)^[48]:

$$\lambda_e(\theta, T) = \frac{1 - \theta}{1 + 2\theta} \lambda_{efd}(T) \quad [6]$$

In this study, the sintered compact consists of three elements (W, Ni, and Fe); however, tungsten is present in a high content, up to 85 pct of the total volume. In order to simplify calculating, only a tungsten powder compact is taken into consideration. The material

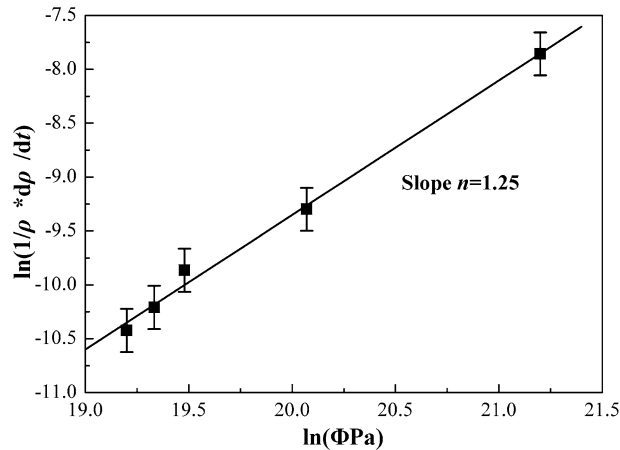


Fig. 9—Stress intensification factor exponent during the intermediate stage.

properties data for tungsten are shown in Table III. The electric field is assumed to be $E = 600 \text{ V m}^{-1}$ (cf. maximum applied voltage of 3 V over the approximate sample height of 5 mm), $\Delta t = 12 \times 3.3 = 39.6$ ms, and the starting temperature $T_0 = 873 \text{ K}$ ($600 \text{ }^\circ\text{C}$). Thus, by assuming the pore radius $r_p = 1 \text{ } \mu\text{m}$, depending on the sintering temperatures and material properties data for tungsten, the calculation result from Eq. [4] is plotted in Figure 10.

The local temperature gradient reaches the level of 10^6 K/m and decreases with increasing the dwell time. Thus, there is a possibility of the local temperature gradient in the vicinity of the pores to result in melting or softening of nickel and iron. The assumption that a viscous layer coated the tungsten particles discussed before is also acceptable. Furthermore, the local thermal gradient improves the solubility of W into the γ -(Ni, Fe) matrix and the results are shown in Table II, where the solubility of W in the matrix phase is stable, and about 32 wt pct regardless of the sintering temperature, is reasonably explained. The particles are subjected to the externally applied stress, allowing the viscous contiguity at the W particle interfaces. In such a case, densification of the heavy alloy powder compact may take place by W grain rotation and sliding, which are often described in terms of viscous process. This mechanism has been proven when a viscous layer at the grain surfaces during the SPS of YAG ceramics.^[51] Thus, grain rotation may be an accommodation mechanism, proceeding *via* diffusion through the viscous matrix phase.

Accompanying densification during sintering process, another phenomenon is grain growth. The grain growth

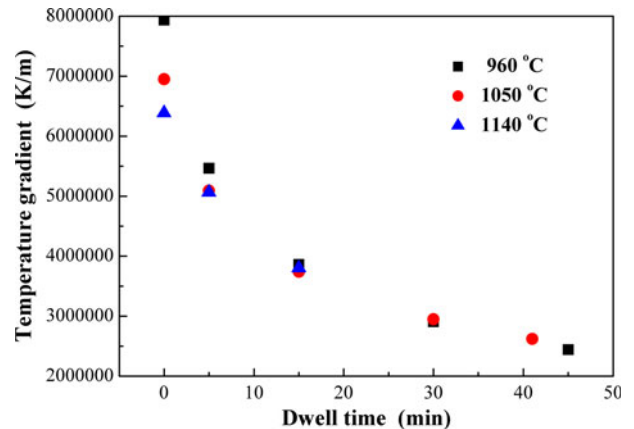


Fig. 10—Local temperature gradients in the vicinity of pores as a function of the dwell time at different sintering temperatures.

Table III. Properties Data for Tungsten

Properties	Tungsten
Electrical Conductivity λ_{efd} ($\mu\Omega^{-1} \mu\text{m}^{-1}$) at 423 K to 1723 K ($150 \text{ }^\circ\text{C}$ to $1450 \text{ }^\circ\text{C}$) ^[49]	$\lambda_{efd} = 1/\rho_e = 1/(-0.021 + 2.467 \times 10^{-4}T + 1.201 \times 10^{-8}T^2)$
Heat Capacity C_{fd} ($\text{J mol}^{-1} \text{ K}^{-1}$) at 300 K to 3500 K ($27 \text{ }^\circ\text{C}$ to $3227 \text{ }^\circ\text{C}$) ^[50]	ρ_e is electrical resistivity $C_{fd} = \sum_{n=-1}^3 A_n \left(\frac{T}{1000}\right)^n$ $A_{-1} = -0.20869, A_0 = 23.70345, A_1 = 5.132062,$ $A_2 = -1.99922, A_3 = 0.734168, (1 \text{ mol} = 183.85 \text{ g})$

of tungsten heavy alloys is generally treated by variants of Ostwald ripening theory, in which the coarsening is accomplished by the dissolution and precipitation mechanism. It has also been reported that nickel as an additive can reduce the recrystallization temperature and enhance the grain growth of the recrystallized material in tungsten wires at 1473 K to 1673 K (1200 °C to 1400 °C).^[52] Following the microstructural observations as shown in Figure 11, the rounded shape of the W–matrix interface suggests that the main grain growth during the intermediate stage is controlled by the dissolution-precipitation process. On the other hand, the coalescence of W grains takes place when increasing dwell time (as shown by the arrows in Figure 11). In the viscous process, grains rotate or slide relative to their adjacent grains to lower their grain boundary energy, which can result in grain coalescence. Therefore, possible grain boundary diffusion also can contribute to the grain growth. Additionally, a high proportion of free surface may be active for grain growth *via* surface diffusion when relative density is low at lower temperature [*i.e.*, porosity is about 15 pct after soaking 41 minutes at 1323 K (1050 °C)]. By using the master sintering curve (MSC) method to analyze the grain growth of tungsten heavy alloys, Park *et al.*^[24] found that in the solid state, a mechanism other than Ostwald ripening contributes to grain growth. From the above,

thus, the grain growth in the intermediate stage may be dominated by three mechanisms: Ostwald ripening, grain boundary diffusion, and surface diffusion.

C. Final Stage

During the final stage, the density presents a trend of stalemated even decrease, while the grain size increases dramatically (Figure 8). It is generally observed that the pores are isolated and closed off, and particularly, they are located at grain boundaries or triple junctions (as shown by the arrows in Figure 12). The gas is entrapped in the pores, and during heating, the pressure of the gas increases. As a result, the pores stop shrinking or even coarsening when the gas pressure reaches a critical value (Figure 12). Accordingly, these isolated pores will move together with the grain boundary during grain growth. Therefore, the relative mobility of pores compared with boundary mobility will determine the microstructure development. Because grain growth mechanisms are not influenced by the applied mechanical pressure during HP or SPS, the grain growth rate can be approximated by a derived model of “pore-dragged” as proposed by Kang.^[53]

$$\frac{1}{G} \frac{dG}{dt} = \frac{K}{RTG^j(1-\rho)^j} \quad [7]$$

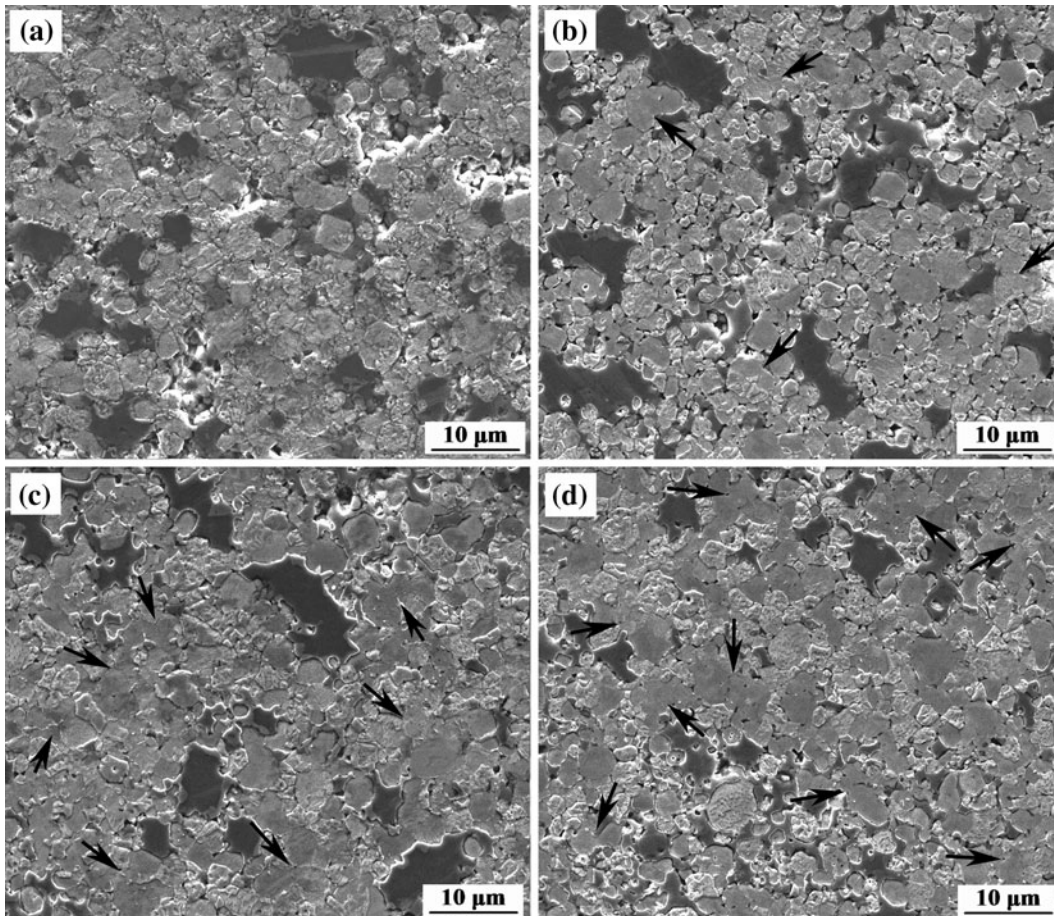


Fig. 11—Microstructure evolution of W-Ni-Fe sintered at 1323 K (1050 °C) for (a) 5 min, (b) 15 min, (c) 30 min, and (d) 41 min. The heating rate was fixed at 90 K min⁻¹ (90 °C min⁻¹) and a constant pressure of 30 MPa was applied. Arrows indicate the coalescence of W grains.

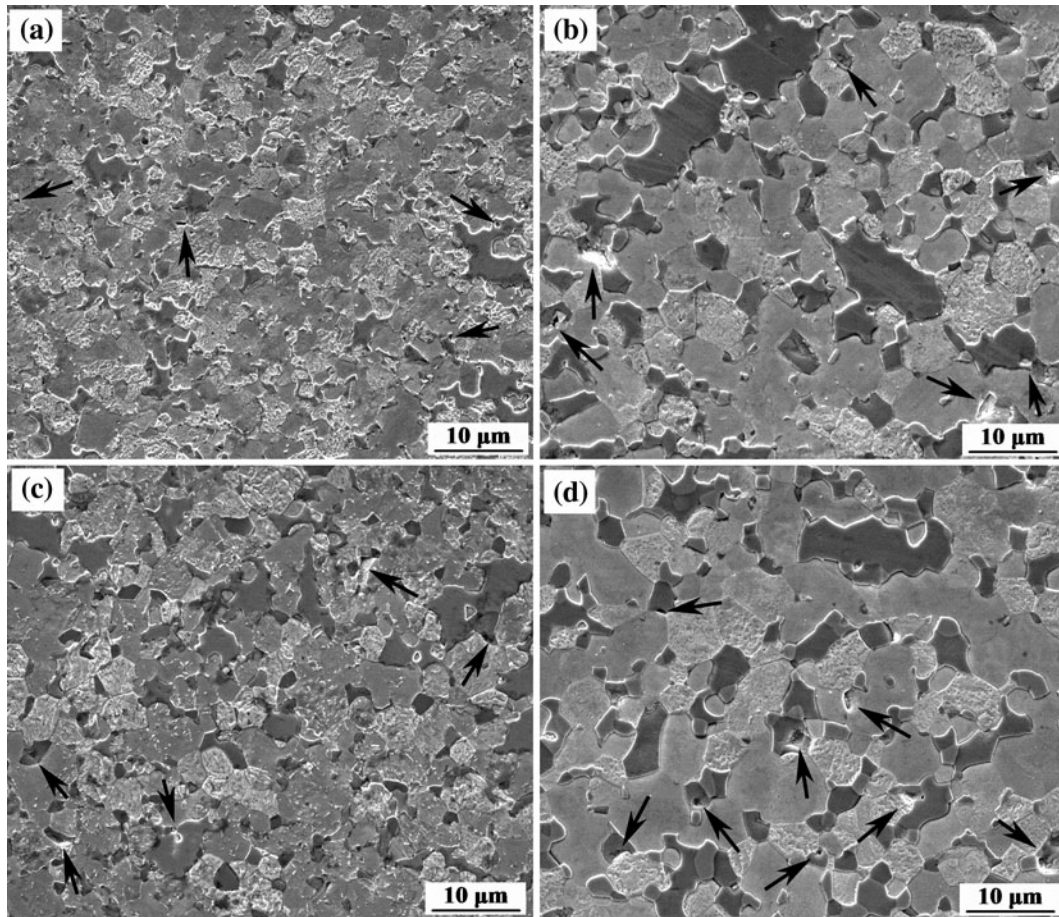


Fig. 12—Microstructure evolution at the final stage of W-Ni-Fe sintered at 1503 K (1230 °C) for (a) 5 min and (b) 45 min and at 1593 K (1320 °C) for (c) 5 min and (d) 45 min. The heating rate was fixed at 90 K min⁻¹ (90 °C min⁻¹) and a constant pressure of 30 MPa was applied. Arrows indicate the presence of intergranular and triple junction pores.

where K is a constant containing various parameters (diffusivity, surface energy, molar volume); and G , R , T , and ρ have the same definition as in Eq. [1]. The exponents l and j are related to the grain growth mechanism. For a given density and temperature, plotting

$$\ln\left(\frac{1}{G} \frac{dG}{dt}\right)$$

vs $\ln(G)$ allows the evaluation of the grain size exponent and, thus, the grain growth mechanism. Figure 13 depicts the W grain growth rates vs the normalized grain size during the final stage (where the relative density is about 0.96). According to this analysis, a high value of grain size exponent for the growth rate $l \approx 3$, and the grain growth during the final stage seems to be controlled by gas phase diffusion.^[53] Unfortunately, in literature,^[53] Kang did not give any possible explanation to this mechanism. However, the thermal gradients in the vicinity of pores may promote the gas atom transport. Otherwise, because the driving force of grain growth is the decrease in free energy of the grain boundary region, it can be supposed that the thermal gradients in the vicinity of pores can also

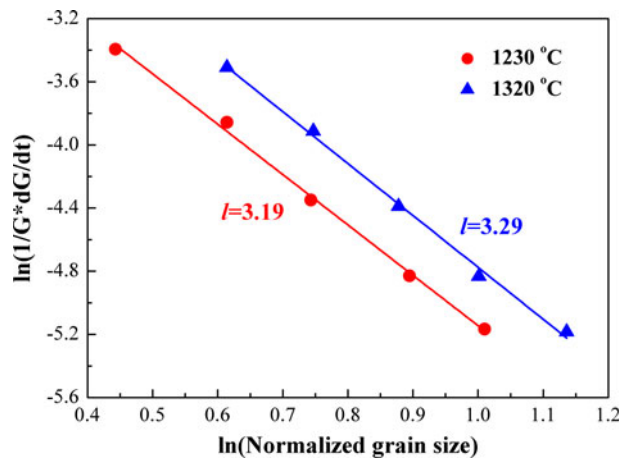


Fig. 13—Grain growth kinetics during the final stage.

enhance the grain growth. This hypothesis, however, requires more advanced experimental investigations to confirm or invalidate it. On the other hand, when fast grain growth dominates over the densification, Eq. [7] can be rewritten as a general format

$$\frac{dG}{dt} = \frac{K}{RTG^{l-1}} \quad [8]$$

Substituting $l = 3$ into Eq. [8] and integrating it, then

$$G^3 - G_0^3 = \frac{K}{RT} t \quad [9]$$

is obtained, where t is the dwell time at sintering temperature T and G_0 is the grain size at $t = 0$ min. According to the literature,^[24] Eq. [9] is associated to a dissolution and precipitation mechanism of the grain growth of tungsten heavy alloys. As mentioned above, the grain growth may be controlled by both the gas phase diffusion and dissolution–precipitation mechanisms. As a result, in the final stage, grain growth predominates and densification stagnates, as shown in the sintering trajectory (Figure 8).

V. CONCLUSIONS

Blended 93W-5.6Ni-1.4Fe powders were sintered via the SPS method with various parameters such as sintering temperature and dwell duration. Based on a detailed report on microstructure development and by means of classical kinetics laws, the densification and grain growth behavior are analyzed. The conclusions can be summarized as follows:

1. The local temperature gradient in the vicinity of the pores creates a possibility of melting or softening of the matrix phase, resulting in the W grains coated by a viscous layer and an improved solubility of W into the matrix phase.
2. Particle rearrangement and neck formation and growth are dominating in the initial stage ($\rho < 0.65$). The γ -(Ni, Fe) matrix phase has formed in this stage. Applied pressure and particular “SPS effect” may enhance the neck formation and growth.
3. In the intermediate stage, dissolution–precipitation of W grains in the viscous matrix phase and Ni-enhanced grain boundary diffusion with viscous process (grain rotating and sliding) dominate the simultaneous densification and grain growth.
4. During the final stage, grain growth predominates and densification stagnates. The grain growth is controlled through both the gas phase diffusion and dissolution-precipitation mechanisms.

ACKNOWLEDGMENTS

This work was supported by the National Basic Research Program of China (No. 2010CB635104), the National Nature Science Foundation (No. 51174095), the Fundamental Research Funds for the Central Universities (No. 2012ZG0006), and the Program for New Century Excellent Talents in University (No. NCET-10-0364).

REFERENCES

1. Y. Yu, E.D. Wang, and L.X. Hu: *Mater. Sci. Technol.*, 2006, vol. 14, pp. 385–89.
2. S.H. Hong and H.J. Ryu: *Mater. Sci. Eng. A*, 2003, vol. 344, pp. 253–60.
3. Y.B. Zhu, Y. Wang, X.Y. Zhang, and G.W. Qin: *Int. J. Refract. Met. Hard Mater.*, 2007, vol. 25, pp. 275–79.
4. R.M. German: *Sintering Theory and Practice*, Wiley, New York, NY, 1996.
5. W.D. Cai, Y. Li, R.J. Dowding, F.A. Mohamed, and E.J. Lavernia: *Rev. Particulate Mater.*, 1995, vol. 3, pp. 71–131.
6. S. Raghunathan and D.L. Bourell: *P/M Sci. Technol. Briefs*, 1999, vol. 1, pp. 9–14.
7. J.L. Fan, B.Y. Huang, and X.H. Qu: *Trans. Nonferrous Met. Soc. China*, 2000, vol. 10, pp. 57–59.
8. W.E. Gurwell: *Proc. International Conference on Tungsten Refract Met-1994*, A. Bose and R.J. Dowding, eds., MPIF, Princeton, NJ, 1994, pp. 65–75.
9. T.H. Sylvia, H. Thomas, and S. Theador: *Proc. International Conference on Tungsten Refract Met-1994*, A. Bose and R.J. Dowding, eds., MPIF, Princeton, NJ, 1994, pp. 169–76.
10. H.J. Ryu, S.H. Hong, and W.H. Baek: *J. Mater. Process. Technol.*, 1997, vol. 63, pp. 292–97.
11. H.J. Ryu and S.H. Hong: *Mater. Sci. Eng. A*, 2003, vol. 363, pp. 179–84.
12. G.C. Wu, Q. You, and D. Wang: *Int. J. Refract. Met. Hard Mater.*, 1999, vol. 17, pp. 299–304.
13. S.H. Hong, S.L. Kang, D.N. Yoon, and W.H. Baek: *Metall. Trans. A*, 1991, vol. 22A, pp. 1969–74.
14. S. Park, D.K. Kim, S. Lee, H.J. Ryu, and S.H. Hong: *Metall. Mater. Trans. A*, 2001, vol. 32A, pp. 2011–20.
15. K.H. Lee, S.I. Cha, H.J. Ryu, and S.H. Hong: *Mater. Sci. Eng. A*, 2007, vol. 458, pp. 323–29.
16. A. Upadhyaya, S.K. Tiwari, and P. Mishra: *Scripta Mater.*, 2007, vol. 56, pp. 5–8.
17. G. Prabhu, A. Chakraborty, and B. Sarma: *Int. J. Refract. Met. Hard Mater.*, 2009, vol. 27, pp. 545–48.
18. X.Q. Li, H.W. Xin, K. Hu, and Y.Y. Li: *Trans. Nonferrous Met. Soc. China*, 2010, vol. 20, pp. 443–49.
19. J.R. Groza: *Met. Powder Rep.*, 2000, vol. 55, pp. 16–18.
20. S. Kandukuri: *Met. Powder Rep.*, 2008, vol. 63, pp. 22–27.
21. K. Hu, X. Li, C. Yang, and Y. Li: *Trans. Nonferrous Met. Soc. China*, 2011, vol. 21, pp. 493–501.
22. J. Räthel, M. Herrmann, and W. Beckert: *J. Eur. Ceram. Soc.*, 2009, vol. 29, pp. 1419–25.
23. A. Zavaliangos, J. Zhang, M. Krammer, and J.R. Groza: *Mater. Sci. Eng. A*, 2004, vol. 379, pp. 218–28.
24. S.J. Park, J.M. Martin, J.F. Guo, J.L. Johnson, and R.M. German: *Metall. Mater. Trans. A*, 2006, vol. 37A, pp. 3337–46.
25. *Standard Test Methods for Determining Average Grain Size*, ASTM Designation E112-96, ASTM, Philadelphia, PA, 1996, p. 16.
26. U. Anselmi-Tamburini, J.E. Garay, and Z.A. Munir: *Mater. Sci. Eng. A*, 2005, vol. 407, pp. 24–30.
27. Y. Aman, V. Garnier, and E. Djurado: *J. Mater. Sci.*, 2012, vol. 47, pp. 5766–73.
28. A. Cordier, M. Kleitz, and M.C. Steil: *J. Eur. Ceram. Soc.*, 2012, vol. 32, pp. 1473–79.
29. D. Demirskyi, H. Borodianska, D. Agrawal, A. Ragulya, Y. Sakka, and O. Vasylykiv: *J. Alloys Compd.*, 2012, vol. 523, pp. 1–10.
30. J.M. Frei, U. Anselmi-Tamburini, and Z.A. Munir: *J. Appl. Phys.*, 2007, vol. 101, pp. 114914–21.
31. N. Toyofuku, T. Kuramoto, T. Imai, M. Ohyanagi, and Z.A. Munir: *J. Mater. Sci.*, 2012, vol. 47, pp. 2201–05.
32. S.J. Park, J.M. Martin, J.F. Guo, J.L. Johnson, and R.M. German: *Metall. Mater. Trans. A*, 2006, vol. 37A, pp. 2837–48.
33. C. Chausse and F. Nardou: *Mater. High Temp.*, 1999, vol. 16, pp. 37–41.
34. M. Gendre, A. Maître, and G. Trolliard: *Acta Mater.*, 2010, vol. 58, pp. 2598–2609.
35. J. Langer, M.J. Hoffmann, and O. Guillon: *Acta Mater.*, 2009, vol. 57, pp. 5454–65.
36. J. Langer, M.J. Hoffmann, and O. Guillon: *J. Am. Ceram. Soc.*, 2011, vol. 94, pp. 24–31.

37. J. Langer, M.J. Hoffmann, and O. Guillon: *J. Am. Ceram. Soc.*, 2011, vol. 94, pp. 2344–53.
38. S.-J.L. Kang: *Sintering, Densification, Grain Growth and Microstructure*, Elsevier Butterworth Heinemann, Oxford, U.K., 2005, pp. 39–56.
39. R.L. Coble: *J. Appl. Phys.*, 1970, vol. 41, pp. 4798–4807.
40. K. Wang, Z. Fu, W. Wang, Y. Wang, J. Zhang, and Q. Zhang: *J. Mater. Sci.*, 2007, vol. 42, pp. 302–06.
41. X. Song, X. Liu, and J. Zhang: *J. Am. Ceram. Soc.*, 2006, vol. 89, pp. 494–500.
42. D. Demirskyi, H. Borodianska, S. Grasso, Y. Sakka and O. Vasykiv: *Scripta Mater.*, 2011, vol. 65, pp. 683–6.
43. K.R. Anderson, J.R. Groza, M. Fendorf, and C.J. Echer: *Mater. Sci. Eng. A*, 1999, vol. 270, pp. 278–82.
44. J.R. Groza and A. Zavaliangos: *Mater. Sci. Eng. A*, 2000, vol. 287, pp. 171–77.
45. Z.A. Munir, D.V. Quach, and M. Ohyanagi: *J. Am. Ceram. Soc.*, 2011, vol. 94, pp. 1–19.
46. M.N. Rahaman: *Ceramics Processing and Sintering*, 2nd ed., Marcel Dekker, New York, NY, 2003, pp. 514–39.
47. L.A. Stanciu, V.Y. Kodash, and J.R. Groza: *Metall. Mater. Trans. A*, 2001, vol. 32A, pp. 2633–38.
48. E.A. Olevsky and L. Froyen: *J. Am. Ceram. Soc.*, 2009, vol. 92, pp. 122–32.
49. B. Wilthan, C. Cagran, and G. Pottlacher: *Int. J. Thermophys.*, 2005, vol. 26, pp. 1017–29.
50. G.K. White and S.J. Collocott: *J. Phys. Chem. Ref. Data*, 1984, vol. 13, pp. 1251–57.
51. R. Chaim, R. Marder-Jaeckel, and J.Z. Shen: *Mater. Sci. Eng. A*, 2006, vol. 429, pp. 74–78.
52. I.H. Moon, K.Y. Kim, S.T. Oh, and M.J. Suk: *J. Alloys Compd.*, 1993, vol. 201, pp. 129–37.
53. S.-J.L. Kang: *Sintering, Densification, Grain Growth and Microstructure*, Elsevier Butterworth Heinemann, Oxford, U.K., 2005, pp. 145–62.